IMAC-XXXIX Feb. 8 – 11, 2021 Orlando, FL, USA
SAND2020-13505C

Pre-test Predictions of Next-Level Assembly Using Calibrated Nonlinear Subcomponent Model

Eric Robbins[1], Trent Schreiber[2], Arun Malla[3],
Benjamin R. Pacini[4], Robert J. Kuether[4], Simone Manzato[5], Daniel R. Roettgen[4], Fernando Moreu[1]

[1]University of New Mexico, Albuquerque, NM, USA
[2]Georgia Institute of Technology, Atlanta, GA, USA
[3]Virginia Polytechnic Institute and State University, Blacksburg, VA, USA
[4]Sandia National Laboratories*, Albuquerque, NM, USA
[5]Siemens Industry Software, Leuven, Belgium

ABSTRACT

A proper understanding of the complex physics associated with nonlinear dynamics can improve the accuracy of predictive engineering models and provide a foundation for understanding nonlinear response during environmental testing. Several researchers and studies have previously shown how localized nonlinearities can influence the global vibration modes of a system. This current work builds upon the study of a demonstration aluminum aircraft with a mock pylon with an intentionally designed, localized nonlinearity. In an effort to simplify the identification of the localized nonlinearity, previous work has developed a simplified experimental setup to collect experimental data for the isolated pylon mounted to a stiff fixture. This study builds on these test results by correlating a multi-degree-of-freedom model of the pylon to identify the appropriate model form and parameters of the nonlinear element. The experimentally measured backbone curves are correlated with a nonlinear Hurty/Craig-Bampton (HCB) reduced order model (ROM) using the calculated nonlinear normal modes (NNMs). Following the calibration, the nonlinear HCB ROM of the pylon is attached to a linear HCB ROM of the wing to predict the NNMs of the next level wing-pylon assembly as a pre-test analysis to better understand the significance of the localized nonlinearity on the global modes of the wing structure.

Keywords: Nonlinear dynamics, nonlinear normal modes, backbone curves, Craig-Bampton reduction, multi-harmonic balance

1. INTRODUCTION

Large deformations, materials, and displacement-dependent boundary conditions are all potential sources of nonlinearity in engineering applications. Effects of nonlinearity on structural dynamic response include internal resonances, amplitude-dependent modal characteristics, self-excited oscillation, and non-repeatability, to name a few. These physics have been studied by numerous researchers for several decades, resulting in major developments towards modeling, analysis, and experimental techniques [1]. While linear models can yield adequate results for predicting and characterizing structural dynamic response, nonlinear effects can influence the accuracy of these models and introduce behavior not supported by linear theory. Including nonlinear physics in engineering models can often improve the model's predictive capability and even provide opportunities for improved performance in design. Adequate modeling relies thoroughly on experimental as well as computational techniques [2].

Sandia National Laboratories is a multimission laboratory managed and operated by National Technology & Engineering Solutions of Sandia, LLC, a wholly owned subsidiary of Honeywell International Inc., for the U.S. Department of Energy's National Nuclear Security Administration under contract DE-NA0003525.

Cooper et al. studied the nonlinear dynamics of a demonstration aluminum aircraft in [3] with intentionally designed, localized nonlinearities. This investigation utilized finite element modeling and experimental test-based identification to extend linear analysis techniques to develop a nonlinear model of the system, following the approach described in [4]. This approach was applied to the demo aircraft depicted in Figure 1.1. On the wings of this structure, the subcomponents representing engine pylon subassemblies were mounted as shown in the red boxes in Figure 1.1, and consisted of two "block" components, a "thin beam," and a swinging "tip mass." Potential sources of nonlinearity marked on the right of Figure 1.1 include: (1) geometric nonlinearity of the thin beam, (2) contact with the blocks, and (3) friction in the bolted connections.

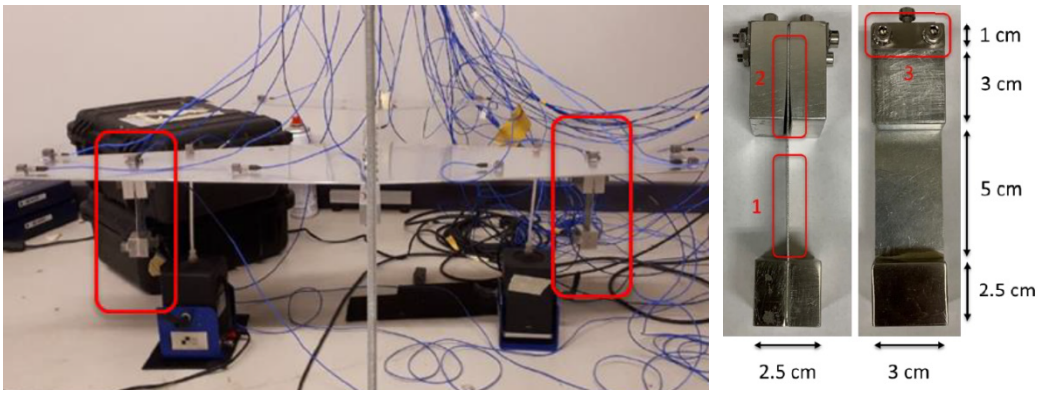

Figure 1.1 (Left) Demo aluminum aircraft test setup from [3]; (right) pylon subassemblies (marked by red boxes)

During the experimental procedures presented in [3], the identification of the nonlinear elements of the pylon proved difficult due to the high modal density of the aircraft structure and the influence of the nonlinearity on the global modes. The results of the initial study motivated further investigations to identify the nonlinearity by removing the pylon, and hence the localized nonlinearity, from the aircraft assembly, and attaching it to a more rigid test fixture with less modal density in the frequency range of interest. The study by Ligeikis et al. performed system identification of this isolated pylon by executing stepped sine and free decay experiments and post-processing the results to identify the frequency and damping backbones of the pylon [5]. The pylon assembly was mounted within a stiff box fixture structure as shown in Figure 1.2. Figure 1.2 (a) shows the overall view of the experimental setup while Figure 1.2 (b) shows a more detailed photograph of the accelerometer locations during the tests. Data collected from these tests were used to develop and validate a single-degree-of-freedom nonlinear model of the pylon and provided motivation for the current research presented in this paper.

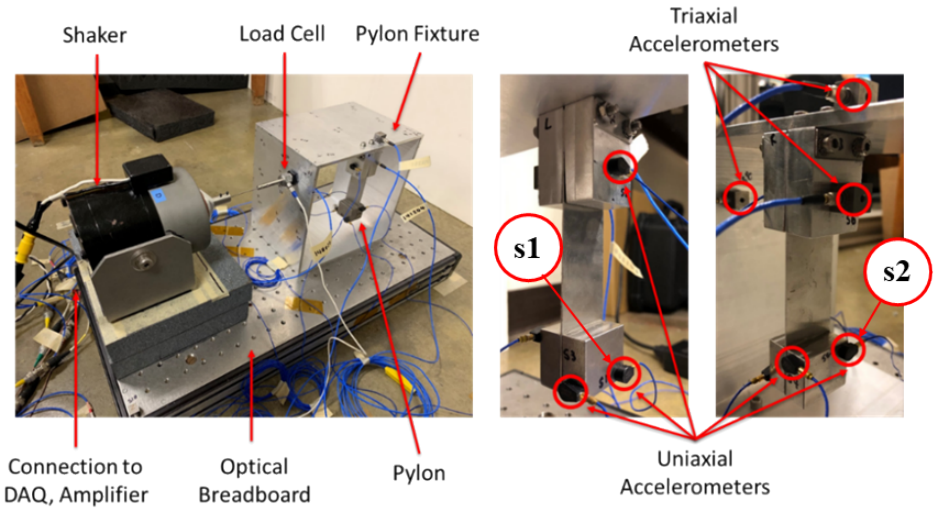

Figure 1.2 Isolated fixture-pylon assembly test setup from [5]

This paper describes the identification of the localized nonlinearity of the isolated pylon structure for a multi-degree-of-freedom (MDOF) representation of the structure. A detailed, linear finite element model was created of the fixture-pylon setup in Figure 1.2, from which a Hurty/Craig-Bampton (HCB) superelement was then created with physical degrees-of-freedom at the location of the nonlinearity [6, 7]. This nonlinear HCB superelement was calibrated using the frequency backbone curves extracted from the experimental results in [5]. The nonlinear normal modes (NNMs) [8] of the HCB model were computed using the multi-harmonic balance (MHB) approach [9], from which the calculated frequency-amplitude curves were correlated with the test data. Different constitutive model forms were explored, and parameters were optimized to determine which model best replicated the test data. The pylon model was further verified by comparing stepped sine simulations to the experimental stepped sine response. The calibrated, nonlinear HCB model of the pylon was next coupled to a linear HCB wing model in order to gain new insight into the behavior of the next-level wing-pylon assembly.

The rest of the paper is organized as follows. Section 2 provides a brief overview of HCB and NNM theory used throughout the identification and analysis efforts. Section 3 presents the post-processing of the stepped sine experimental data from Ligeikis et al. and its utilization in the development and validation of the nonlinear MDOF model of the isolated pylon assembly. Section 4 discusses the results of the next-level assembly study when mounting the calibrated pylon to a wing-like structure. The influence of the nonlinearity on the global modes of the wing are discussed in the context of the resulting NNMs of the assembly. Finally, Section 5 summarizes the conclusions and future work.

2. THEORY

A brief overview of the theory is presented in the following subsections. Section 2.1 describes the HCB methodology deployed to generate the nonlinear ROM of the pylon subassembly. Section 2.2 provides a brief overview of MHB and its use for calculating periodic orbits, or NNMs, of conservative systems.

2.1 Nonlinear Hurty/Craig-Bampton Reduction

Hurty/Craig-Bampton reduction is a method often used to reduce large-scale finite element models to a lower-order, and more manageable scale. It retains the physical coordinates at the interface (boundary) of a structure, which lends itself well to adding nonlinear constitutive elements that can be readily parameterized. The remaining DOFs in the model are reduced with a fixed-interface modal basis. Hurty provided the first development based on fixed-interface and constraint modes [6]. Craig and Bampton [7] simplified Hurty's method, which has been widely adopted due to its accuracy, ease of implementation, and computational efficiency. The Craig-Bampton method is detailed in [10] and summarized here.

The undamped equations of motion for the full physical system with a conservative nonlinear forcing term is written as,

$$\mathbf{M}\ddot{\mathbf{u}} + \mathbf{K}\mathbf{u} + \mathbf{f}_{nl}(\mathbf{u}) = \mathbf{F}(t) \tag{2.1}$$

The transformation matrix, $\boldsymbol{\Psi}_{CB}$, transforms the full physical space DOFs, $\mathbf{u}$, to a reduced space containing fixed-interface modal coordinates, $\boldsymbol{\eta}_{fi}$, and retained boundary DOFs, $\mathbf{u}_b$.

$$\mathbf{u} = \boldsymbol{\Psi}_{CB}\begin{Bmatrix}\boldsymbol{\eta}_{fi}\\ \mathbf{u}_b\end{Bmatrix} \tag{2.2}$$

This results in the transformation into reduced coordinates,

$$\mathbf{M}_{CB}\begin{Bmatrix}\ddot{\boldsymbol{\eta}}_{fi}\\ \ddot{\mathbf{u}}_b\end{Bmatrix} + \mathbf{K}_{CB}\begin{Bmatrix}\boldsymbol{\eta}_{fi}\\ \mathbf{u}_b\end{Bmatrix} + \begin{Bmatrix}\mathbf{0}\\ \mathbf{f}_{nl}(\mathbf{u}_b)\end{Bmatrix} = \mathbf{F}_{CB}(t) \tag{2.3}$$

where

$$\mathbf{M}_{CB} = \mathbf{\Psi}_{CB}{}^{\mathrm{T}}\mathbf{M}\mathbf{\Psi}_{CB} \qquad \mathbf{K}_{CB} = \mathbf{\Psi}_{CB}{}^{\mathrm{T}}\mathbf{K}\mathbf{\Psi}_{CB} \qquad \mathbf{F}_{CB}(t) = \mathbf{\Psi}_{CB}{}^{\mathrm{T}}\mathbf{F}(t) \tag{2.4}$$

In this study, the reduced mass matrix, $\mathbf{M}_{CB}$, and stiffness matrix, $\mathbf{K}_{CB}$, are obtained for the fixture-pylon and wing-pylon assemblies using Sierra Structural Dynamics [11] finite element codes. With the undamped equations of motion in reduced coordinates in Eq. (2.3), a nonlinear restoring force can be added to any boundary DOF, $\mathbf{u}_b$, to obtain the nonlinear undamped equations of motion. Two types of elements were used in Section 3 to explore the effect of the nonlinearity on the NNM backbone curve predicted using MHB, namely cubic spring elements and linear penalty springs.

2.2 Multi-Harmonic Balance

The MHB method is a Fourier-Galerkin mathematical technique to solve for periodic solutions for nonlinear equations of motion [9]. The technique approximates the displacements with periodic solutions represented by a finite number of harmonics in a Fourier series,

$$\mathbf{u}(t) = \frac{\mathbf{c}_0^x}{\sqrt{2}} + \sum_{k=1}^{N_h}\left[\mathbf{s}_k^u \sin(k\omega t) + \mathbf{c}_k^u \cos(k\omega t)\right] \tag{2.5}$$

$$\mathbf{f}_{nl}(\mathbf{u}) = \frac{\mathbf{c}_0^f}{\sqrt{2}} + \sum_{k=1}^{N_h}\left[\mathbf{s}_k^f \sin(k\omega t) + \mathbf{c}_k^f \cos(k\omega t)\right] \tag{2.6}$$

Note that the displacement field, $\mathbf{u}(t)$, can be any set of DOF to describe the dynamics of a system (i.e. physical DOF, modal DOF, etc..). Projecting the Fourier basis onto the nonlinear equations of motion, such as those in Eqns. (2.1) and (2.3), and performing a Galerkin projection onto the periodic functions produces the frequency-domain equations of motion

$$\mathbf{A}(\omega)\mathbf{z} + \mathbf{b}(\mathbf{z}) = \mathbf{0} \tag{2.7}$$

where $\mathbf{z}$ is the collection of Fourier coefficients, $\mathbf{A}(\omega)$ is the linear dynamic stiffness matrix, and $\mathbf{b}(\mathbf{z})$ is the nonlinear restoring force.

The algorithm is coupled with pseudo-arclength continuation to follow a branch of periodic solutions which is initialized by a starting guess based on the low-energy, linearized modes of the system [12]. The pseudo-arclength continuation technique is used with a Newton solver to find periodic solutions by satisfying a residual function

$$\mathbf{R}(\mathbf{z},\omega) = \begin{bmatrix} \mathbf{A}(\omega)\mathbf{z} + \mathbf{b}(\mathbf{z}) \\ \mathbf{V}^{\mathrm{T}}\left(\begin{Bmatrix}\mathbf{z}\\ \omega\end{Bmatrix} - \begin{Bmatrix}\mathbf{z}\\ \omega\end{Bmatrix}^{(k=1)}\right) \end{bmatrix} \tag{2.8}$$

where $\mathbf{V}$ represents the tangent prediction vector. Each value of $\mathbf{z}$ and ω that solve $\mathbf{R}(\mathbf{z},\omega) = \mathbf{0}$ represents an NNM solution along the branch.

3. FIXTURE-PYLON MODEL CALIBRATION

This section describes the calibration efforts of the nonlinear HCB model of the *fixture-pylon* assembly (Section 3.1). This was accomplished by extracting the amplitude dependent frequency backbone curve from the experimental stepped sine data of the fixture-pylon assembly from [5] (Section 3.2). This data was used with the nonlinear HCB model of the test assembly to evaluate different nonlinear element model forms and select the most appropriate (Section 3.3). The calibrated nonlinear pylon model was further validated by comparing the experimental stepped sine data to the simulated response of the model (Section 3.4).

3.1 Fixture-Pylon Finite Element Model

A detailed finite element model (FEM) of the fixture-pylon assembly was used to create an initially linear HCB model. The mesh of the finite element model was generated using CUBIT [13] and the Sierra Structural Dynamics codes [11] were used for the eigenvalue analysis and HCB reduction. An eigenvalue analysis was performed on the fixture-pylon assembly with a fixed base to determine the linear natural frequencies and mode shapes, such as the first mode shown in Figure 3.1b. This first mode is the 'swinging pendulum' mode of the pylon, with a natural frequency of 7.3 Hz. This was the target mode for the experiments conducted in Ligeikis et al. [5] and was used to characterize the nonlinearity between the thin beam and block.

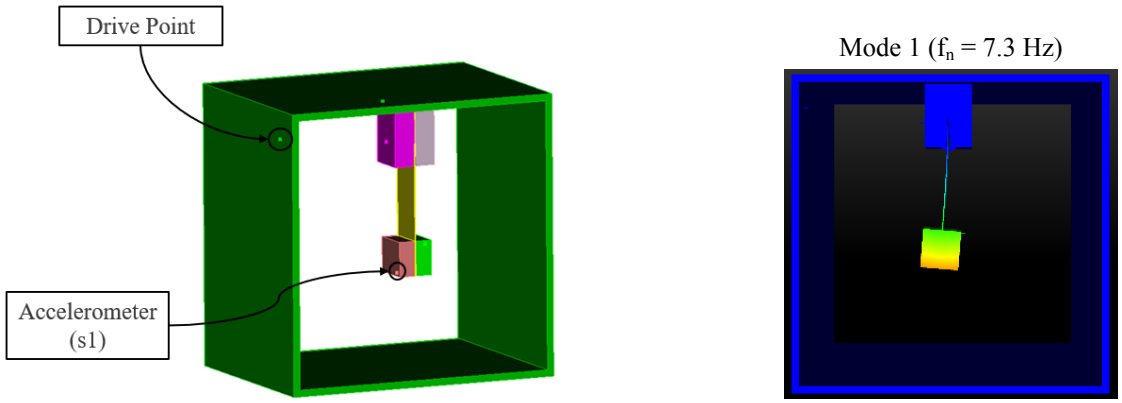

Figure 3.1 Fixture-pylon CAD assembly; (a) general view; (b) natural frequency and mode shape for mode 1

The linear ROM was generated from an HCB reduction with 16 fixed-interface modes and retained seven physical DOFs (drive point, accelerometer s1, accelerometer s2, and four virtual nodes). To account for the nonlinearity, a whole joint modeling approach [14] was used to constrain the finite element nodes along the contact edge of the block to a single, virtual node as shown in Figure 3.2; an analogous whole joint is created along a node line along the thin beam. The nonlinearity localized within the pylon block was modeled as a 1-D constitutive element between the virtual node pairs, resulting in the nonlinear HCB model.

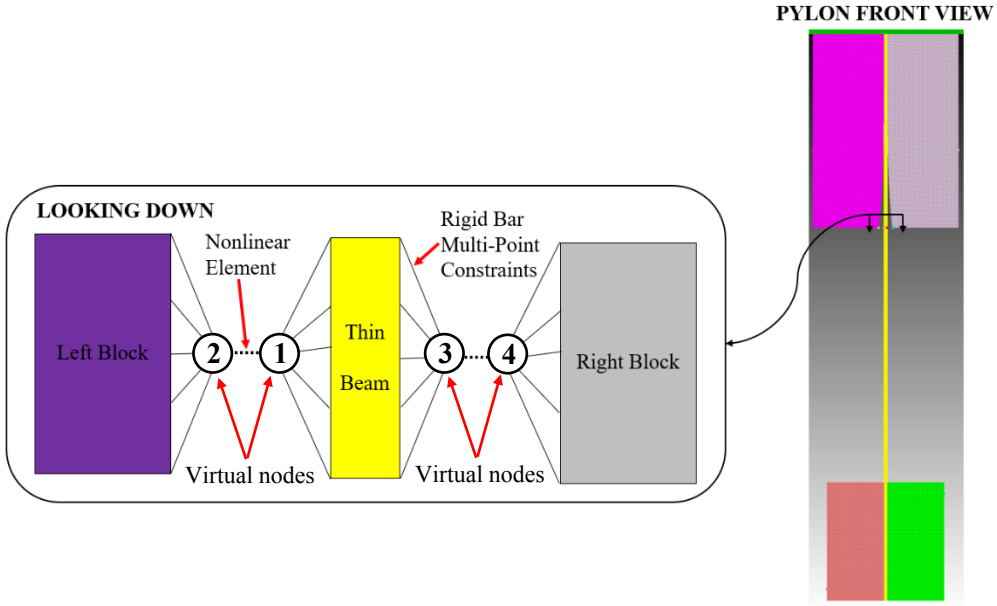

Figure 3.2 Nonlinear element in pylon block

3.2 Extracting Backbone Curves from Experimental Stepped Sine Data

Experimental data was used from stepped sine excitation tests presented in [5]. These tests recorded the system's steady-state response to sinusoidal forcing over a range of discrete frequencies and forcing amplitudes, testing a single frequency and amplitude at a time. This results in a nonlinear force response (NLFR) curve for each forcing amplitude. Compared to other techniques such as broadband/burst random excitation, this method results in a higher quality NLFR to observe the influence of nonlinearity on the resonant modes of interest. The experimental stepped sine data was initially recorded by accelerometers s1 and s2 (labeled in Figure 1.2) into a set of accelerance NLFR curves including both real and imaginary components. The data was used to calculate the magnitude and phase angle response at the s1 location for each of the eleven forcing amplitudes (0.5 – 20 N); these plots are shown in Figure 3.3.

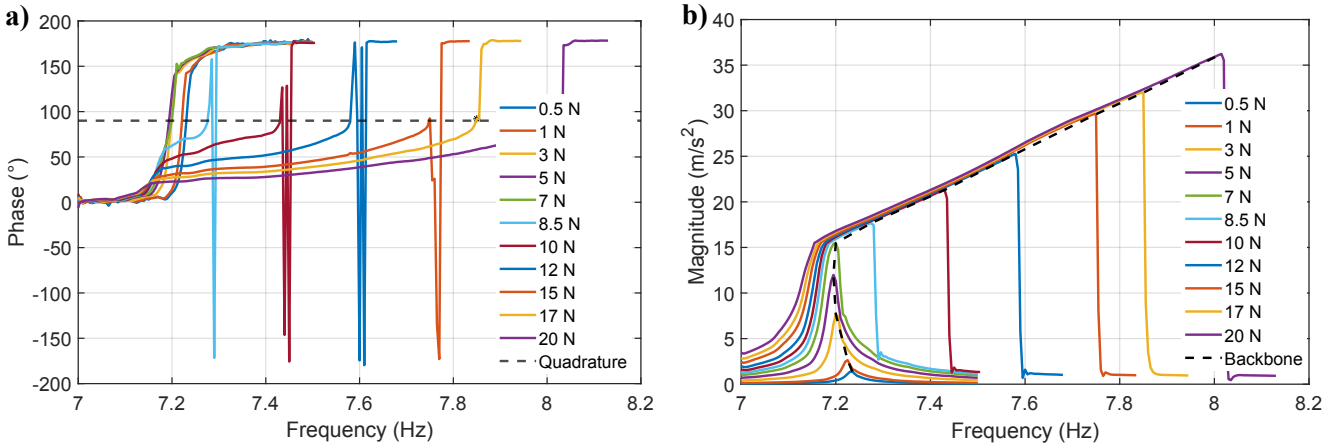

Figure 3.3 Phase (a) and magnitude (b) response spectra at s1 accelerometer point. Dashed line represents quadrature value of 90 degrees in (a) and the backbone curve marked in (b).

The phase resonance condition for nonlinear systems [15] occurs when there is a 90-degree phase difference between the input force and output response. By tracking where this phase quadrature criterion is satisfied between the forcing phase and s1 response phase for each of the forcing amplitudes, the amplitude-dependent resonant frequency of the first bending mode of the pylon can be extracted. The backbone curve is the interpolated curve connecting the quadrature points for the range of forcing amplitudes. It is important to note that perfect quadrature was not achieved during the experimental testing since this was not the original objective of the test efforts. Thus, the points nearest quadrature were used when constructing the backbone curve. The phase angle of these closest points ranged from 81-96°. The final acquired backbone curve, shown in Figure 3.3b, displays an initial weak softening nonlinearity at low forcing amplitudes (0.5 – 7 N), which transitions to a strong hardening behavior as the force level continues to increase (7 – 20 N). This transition coincides with the forcing level at which the thin beam element begins to contact the block elements as the mass swings at higher amplitudes [5]. Reflecting this transition was vital when developing the nonlinear model of the isolated pylon system.

3.3 Calibration of Nonlinear Elements

The interaction between the pylon "block" and "thin beam" components is a significant source of nonlinearity in the fixture-pylon system, as evidenced by the sudden stiffening observed in the experimental backbone curve. A nonlinear constitutive element was added to the HCB model and two constitutive elements were considered for this connection: a cubic spring element and a gap-spring element. These elements were chosen as candidates since both are capable of producing a strong hardening behavior for the frequency backbone curve. The initial softening

behavior was neglected for this effort, as it occurred over a small frequency range that was negligible compared the that of the hardening behavior.

The cubic spring element was connected to the virtual nodes in Figure 3.2 with a restoring force defined as

$$f_{NL}(x_1,x_2) = k_{NL}(x_2 - x_1)^3 \tag{3.1}$$

Here k_{NL} is the nonlinear spring constant and x_1 and x_2 are the displacements of the virtual nodes located on the left side of the thin beam. Since there was no directional dependence on this element, only a single cubic spring was modeled to capture the stiffening effect.

Gap elements were modeled by two linear penalty springs with one each attached to the left and right virtual node connections in Figure 3.2. These springs only applied a restoring force when the relative displacement between the virtual node pairs was sufficient to close the gap. The restoring force for the penalty springs can thus be expressed as

$$f_{gap}(x_i,x_j) = \begin{matrix} k_{pen}(\delta_{ij} - x_{gap})\ for\ \delta_{ij} > x_{gap} \\ 0\ otherwise \end{matrix} \tag{3.2}$$

where k_{pen} was the linear spring constant of the penalty springs, $\delta_{ij} = x_i - x_j$, and x_{gap} is the gap distance of the contact element. The elements were placed between nodes with displacements x_1 and x_2, as well as between x_3 and x_4 to represent the restoring force on the beam/block on each side.

By adding the described nonlinear constitutive elements to the HCB model, a nonlinear reduced order model of the fixture-pylon subassembly was developed using each type of element. Frequency backbone curves were computed for both models using MHB to calculate the NNMs. Figure 3.4 shows the comparison between the experimental backbone curve with the nonlinear HCB ROMs corresponding to the best fit cubic spring and penalty spring elements. Note that these curves are plotted versus the displacement amplitudes at the s1 location and the frequencies are normalized to their respective linear natural frequencies. A parametric study was conducted to determine the set of nonlinear parameters for each model that minimized the error to the experimental backbone. The penalty spring was able to better match the experimental backbone curve and was thus selected as the constitutive element to represent the nonlinearity of the pylon. The penalty spring element was calibrated to the s1 location, and the plot in Figure 3.5 shows the correlation of the backbone at the s2 location, again showing good agreement with both sets of experimental data.

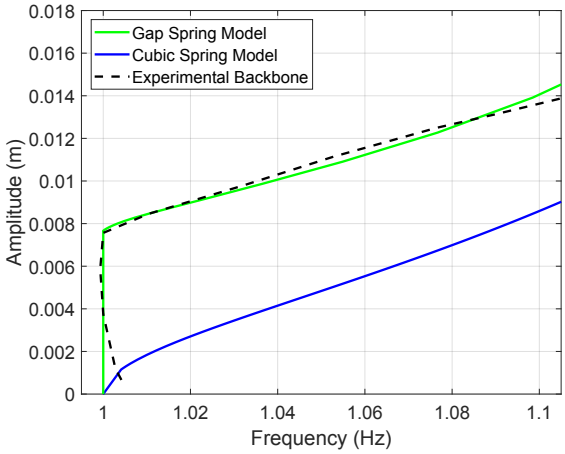

Figure 3.4 Comparison of gap and cubic spring models to experimental backbone (s1 location); parameters: $k_{NL} = 4e10\ N/m$, $k_{pen} = 7e4\ N/m$, and $x_{gap} = 0.68\ mm$

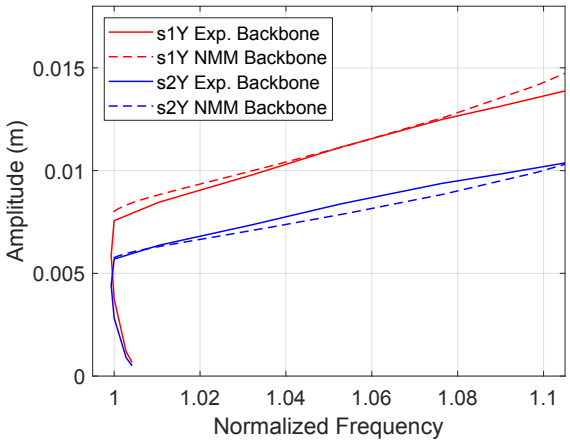

Figure 3.5 Comparison between experimental and NNM backbones for calibrated penalty spring element

3.4 Stepped Sine Validation

Using the calibrated penalty spring elements, a stepped sine simulation was performed to validate the nonlinear HCB model's ability to reproduce the stepped sine experimental data. Rayleigh mass and stiffness proportional damping was used to calculate the damping matrix for the model based on linear damping ratios for modes 1 and 3 [5]. The stepped-sine simulation was conducted by inducing a constant amplitude harmonic force on the fixture drive point node at various oscillating frequencies. The model was integrated using Matlab's ode15s solver to steady state and the response amplitude was recorded as a single point in the NLFR curve. The frequency was incremented with positive frequency steps until the final frequency was reached. This was repeated for several force amplitudes corresponding to the experimental results. The drive point DOF was on the stiff fixture and the output DOF was at the s1 location. The results are shown in Figure 3.6 for the experiment (- - -) and simulation (—) for seven of the 11 forcing amplitudes.

The comparison plots reveal that the amplitude of the simulated data matches well with the experimental data, but the jump-down frequency seems to be in slight disagreement for most amplitudes. The 17 N forcing in the nonlinear response nearly produced an identical response between the simulation and experiment. It can be seen in Figure 3.6 that the linear resonances in the test data were consistently occurring around 1.03, with a slight softening behavior, whereas the linear resonances in the simulation were occurring around 1.045. Some of the most significant differences between the simulation and experimental results may be attributed to the difference in the damping formulation in the model. Here a constant damping ratio is assumed for each mode, however the experiments in [5] reveal that the damping backbone curves are amplitude dependent. The damping is known to influence the resonance condition for NLFR curves, so it is likely that the model is missing the physics to capture this dependence.

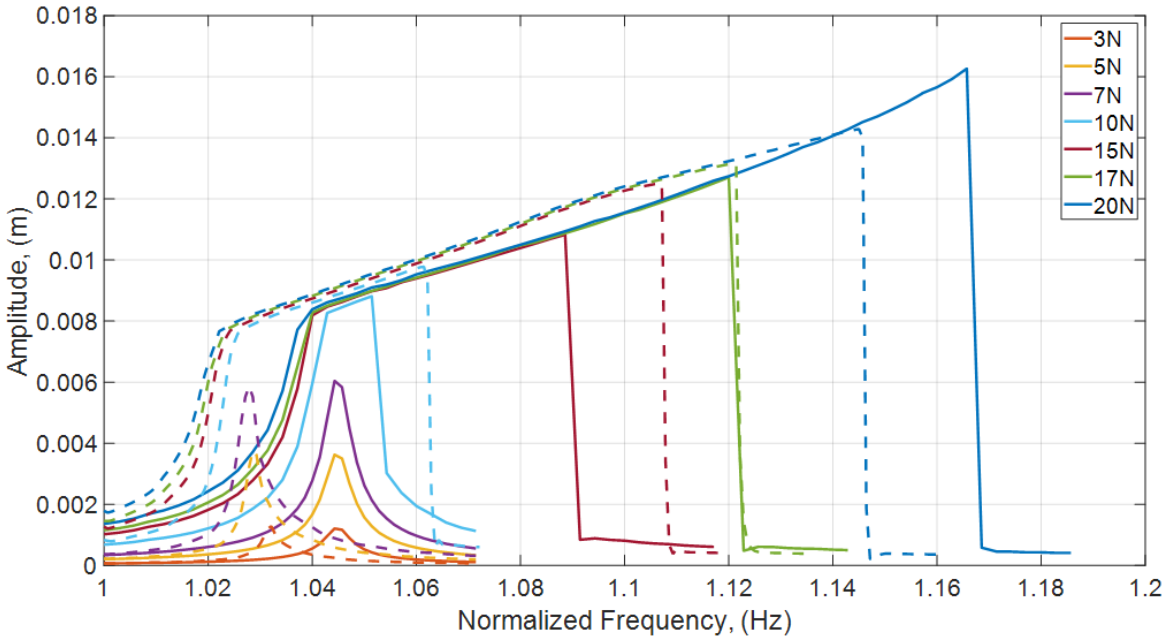

Figure 3.6 Stepped sine test results of fixture-pylon (- - -) experimental (—) simulation

4. WING-PYLON NNM COMPUTATION

This section describes the simulations performed on the nonlinear HCB model of the *wing-pylon-fixture* assembly (Section 4.1). The calibrated nonlinear pylon model from Section 3 was attached to a linear HCB ROM of the wing structure and the NNMs of the next-level assembly are calculated. The first NNM under investigation (Section 4.2) corresponds to the localized mode of the pylon when connected to the wing. The second NNM (Section 4.3) corresponds to the first bending mode of the wing.

4.1 Wing-Pylon Finite Element Model

The mesh of the wing-pylon-fixture assembly was generated using CUBIT [13] and the Sierra Structural Dynamics codes [11] were used for the eigenvalue analysis and HCB reduction. This assembly has free-free boundary conditions. The linear ROM of the wing-pylon-fixture assembly was generated with an HCB reduction that used 30 fixed-interface modes and retained physical DOF for various drive points along the wing and fixture in addition to the same accelerometer and virtual nodes in Section 3.1. The calibrated penalty spring elements between the virtual nodes in the pylon were added to the linear HCB ROM to generate the nonlinear HCB model.

A linear eigenvalue analysis was performed on the wing-pylon-fixture assembly to obtain the linear natural frequencies and mode shapes without the inclusion of the penalty springs. Figure 4.1 shows the elastic modes of interest for the model, in which modes 1 and 2 are the starting points for the NNM computations in Sections 4.2 and 4.3, respectively. The first mode of the wing-pylon-fixture assembly (7.3 Hz) is a localized first bending mode of the pylon and is the same as the first mode of the fixture-pylon assembly that was used to calibrate the nonlinear element. The second mode is a combination of bending in the wing and swinging of the pylon mass at a resonant frequency of 22.2 Hz. The seventh mode imparts torsional motion in the wing and higher order bending of the pylon at 102.1 Hz. This mode is included to help explain the modal interactions that occur within the next-level assembly.

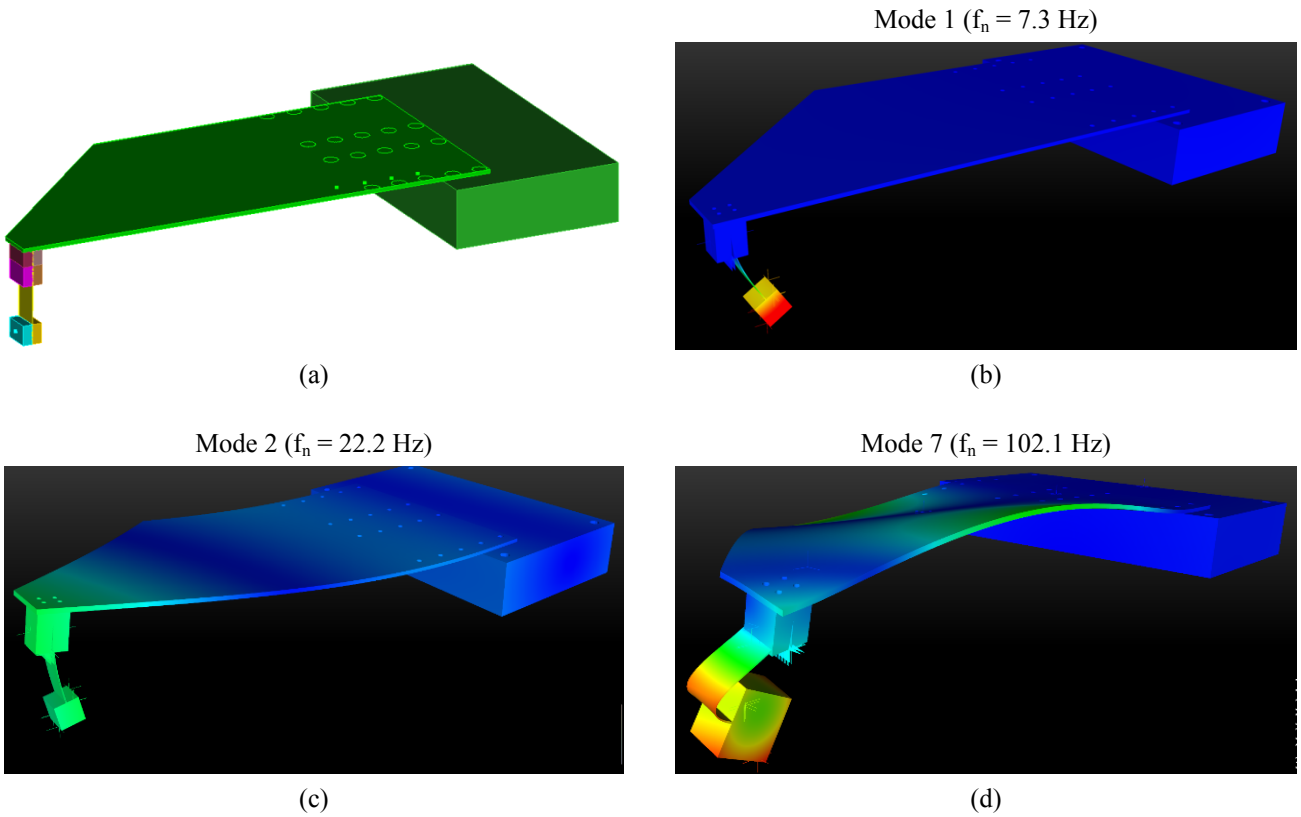

Figure 4.1 Wing-pylon CAD assembly (a) and mode shapes/frequencies for mode 1 (b), mode 2 (c), and mode 7 (d)

4.2 NNM 1 Computation

Figure 4.2 shows the corresponding simulated data for NNM 1 which continues from the linearized mode at 7.3 Hz at a low energy level. The NNMs were calculated using MHB with up the 7th harmonic in the Fourier approximation and the frequency-energy plot (FEP) is shown in Figure 4.2 (a) and (b). The FEP for NNM 1 reveals that the penalty spring does not introduce nonlinearity into the dynamic response until about 1E-02 J, at which point the frequency begins to stiffen. As the energy in the NNM increases, the backbone frequency increases until an internal resonance occurs around 7.4 Hz. The tongue occurs just where the NNM 2 FEP (divided by a frequency integer of three) crosses the NNM 1 FEP, indicating that this is a 3:1 modal interaction between NNM 1 and 2. The displacement time-histories shown in Figure 4.2 (c) and (d) show the higher harmonic content of the response on the tongue as the wing tip completes three oscillations during the fundamental period of motion. In this case, the higher frequency content produced by the nonlinearity at the pylon block strongly excites mode 2. Figure 4.2 (e) and (f) show the frequency content of the displacement time-histories for the wing tip and the pylon block, thus confirming the spectral content of the particular periodic orbit.

It is worth noting here the difference between this NNM compared to the NNM of the first bending mode computed from the *fixture-pylon* model in Section 3. This localized mode of the pylon produces nearly equivalent solutions along the main backbone curve, however the dynamics of the next-level assembly clearly influence whether or not the mode can interact with other modes of the system. The introduction of the 3:1 modal interaction is strictly due to the dynamics of the wing structure, thus highlighting the importance of the fixturing when predicting NNMs of a subcomponent. A stiff or rigid frame may simplify the nonlinear dynamics of the structure by avoiding any modal interactions (as motivated by the system in Section 3). This approach may not necessarily reveal the potentially damaging exchanges of energy that could occur within the system where the nonlinearity introduced into the next-level assembly can introduce global nonlinear effects.

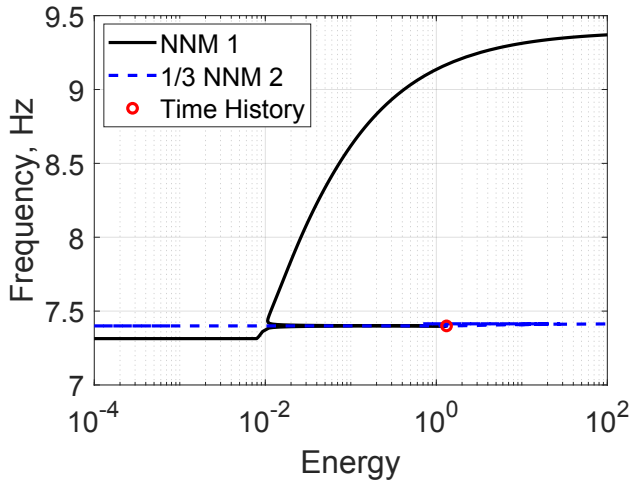

(a)

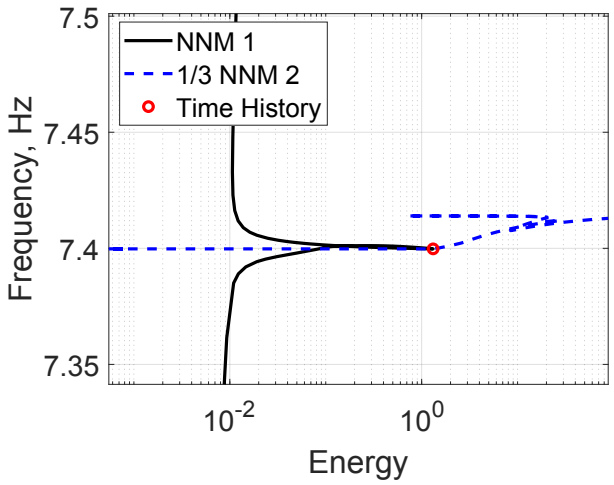

(b)

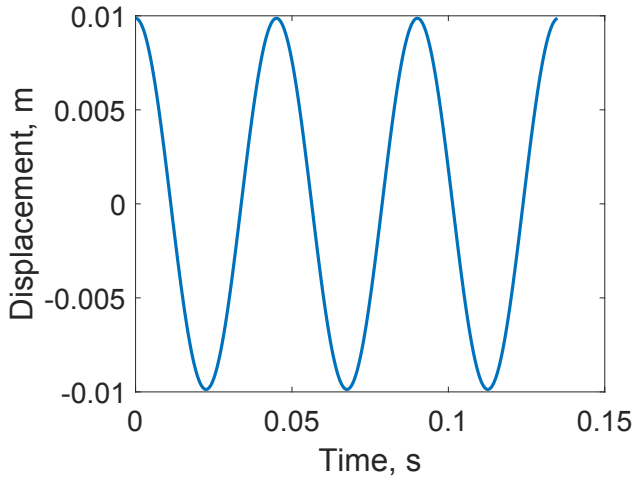

(c)

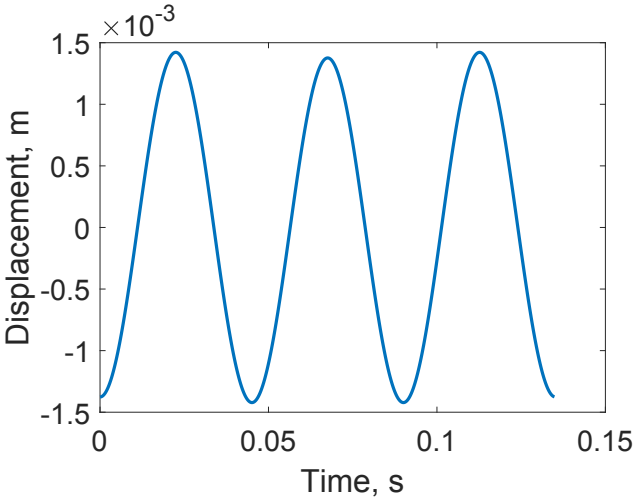

(d)

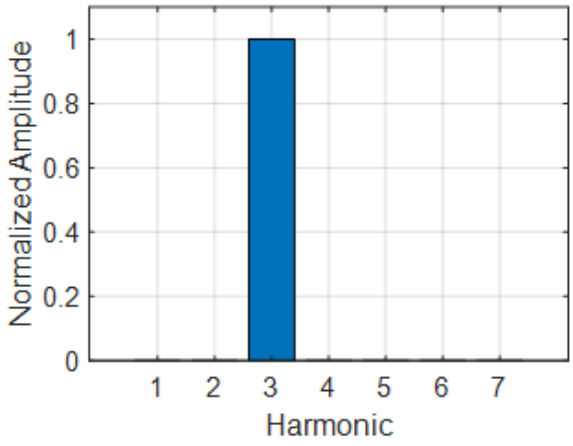

(e)

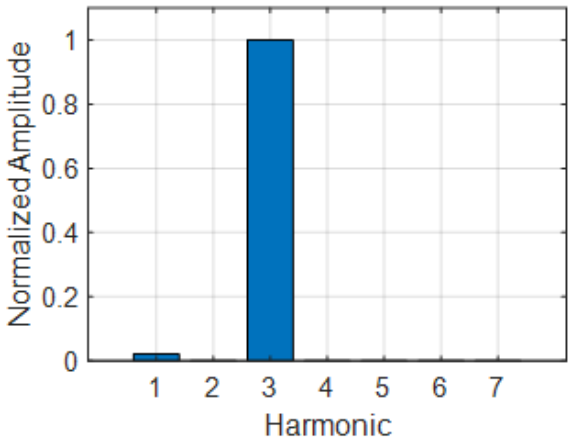

(f)

Figure 4.2 FEP plots for NNM 1 (a) and (b) and the corresponding (red point) displacement time-histories of the s1 node (c) and the wing tip (d). The frequency content of the displacement time histories shown for s1 node (e) and wing tip (f).

4.3 NNM 2 Computation

The simulated data for NNM 2 is shown in Figure 4.3. The NNMs were again calculated using MHB with up the 7th harmonic in the Fourier approximation and the frequency-energy plot (FEP) is shown in Figure 4.3 (a) and (b). The backbone for NNM 2 does not begin to stiffen until approximately 1 J. Over the entire energy range of the computed mode, the penalty spring produces a minimal frequency shift over the operating range, going from 22.2 Hz to about 22.25 Hz, or about 0.2% increase. This suggests that the localized nonlinearity in the pylon does not significantly shift the frequency of the wing bending mode. A more interesting observation comes from the tongue that emanates along the backbone. The backbone crossings of NNM 2 with NNM 7 (divided by a frequency integer of five) are shown in Figure 4.3 (a) and (b), indicating a 5:1 modal interaction. The displacement time histories shown in Figure 4.3 (c) and (d) correspond to the tip of the internal resonance where the pylon completes five oscillations in one oscillation on the wing tip. Figure 4.3 (e) and (f) show the frequency content of the displacement time histories for the wing tip and the pylon block, thus highlighting the dominant frequency content of the motion.

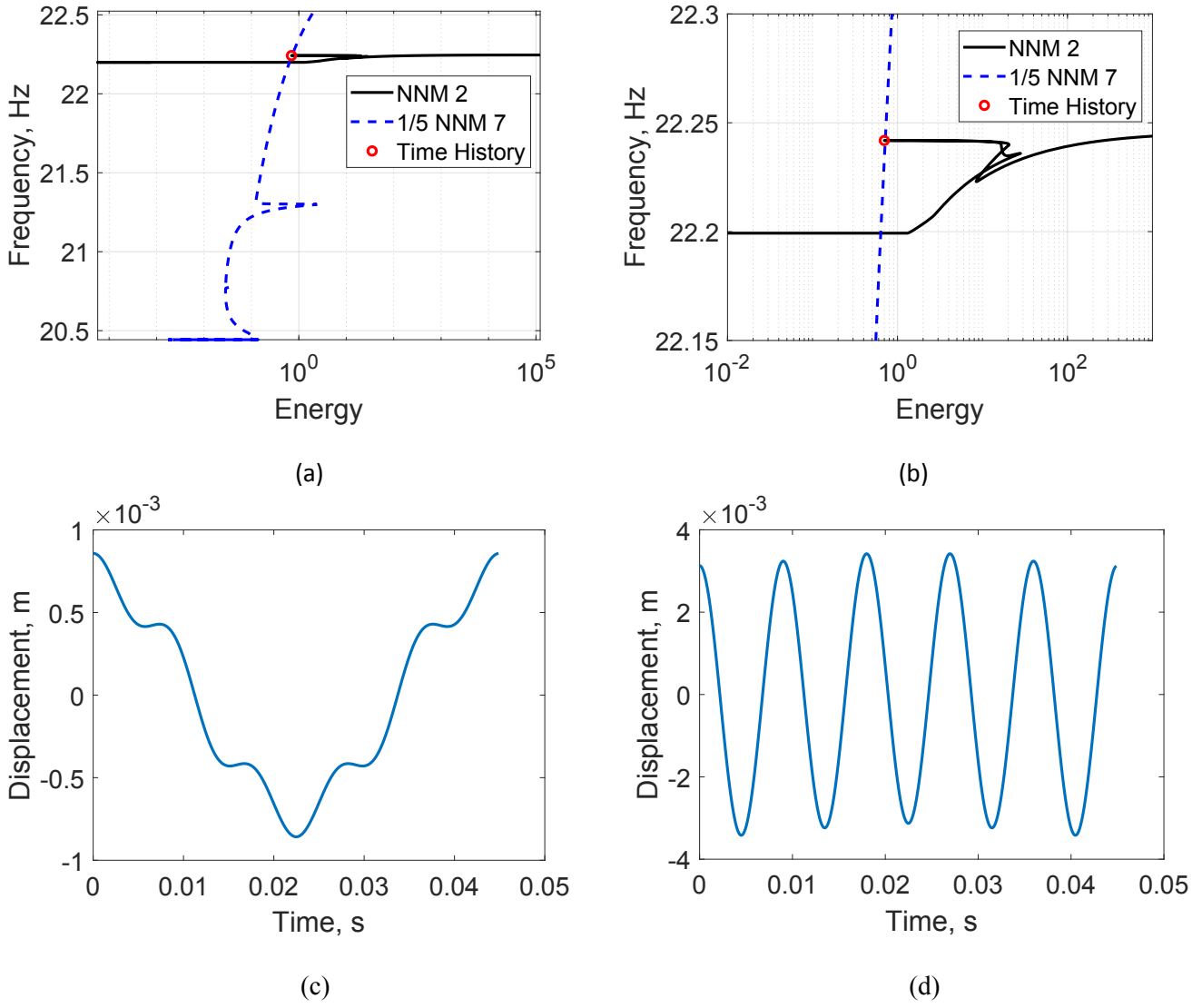

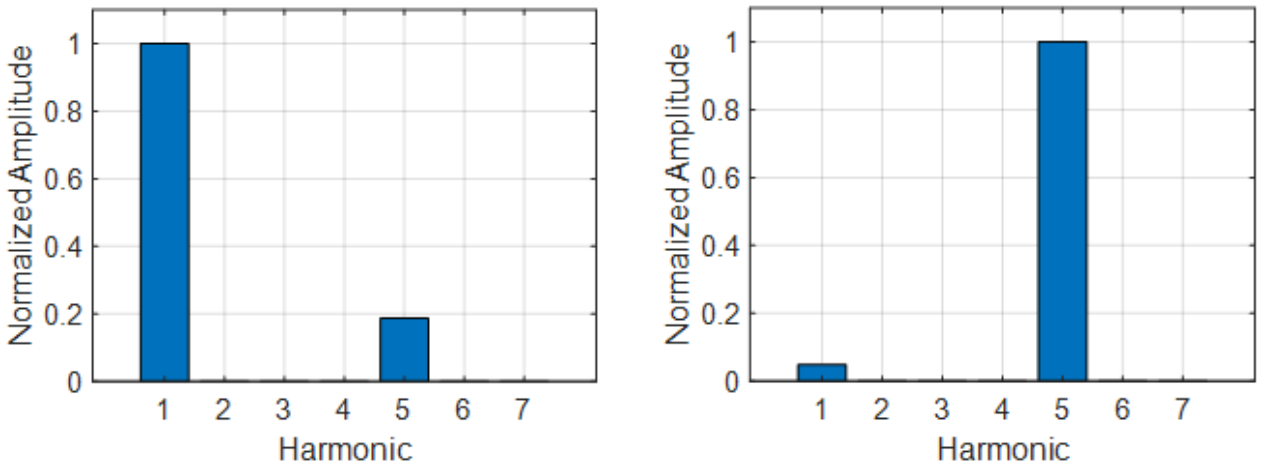

(e) (f)

Figure 4.3 FEP plots for NNM 2 (a) and (b) and the corresponding (red point) displacement time-histories of the s1 node (c) and the wing tip (d). The frequency content of the displacement time histories shown for s1 node (e) and wing tip (f).

It is interesting to observe the relative effect (or lack thereof) of the penalty spring on the backbone frequency of the wing bending mode, i.e. NNM 2. This mode could be effectively assumed to be linear in practice if it not for the presence of the modal interaction with NNM 7. NNM theory provides the theoretical foundation to understand the conditions required for modes to interact, and thus reinforces that it does not necessarily require the mode to have a significant shift in frequency. A modal interaction may occur when a higher frequency NNM of the system has a significant shift, thus satisfying the condition that resonant frequencies are commensurate at a given energy level. This highlights the importance of investigating the NNMs of the next-level assembly and how fixturing decisions can introduce (or eliminate) complex behavior in the system. The wing bending mode was demonstrated here to exchange energy with the higher order mode of the pylon (i.e. NNM 7). Additionally, this mode was also able to receive energy exchange from NNM 1 due to the presence of the 3:1 modal interaction in Section 4.2.

5. CONCLUSIONS

This research built upon the experimental study of the isolated fixture-pylon assembly from previous research. A nonlinear reduced order model of their test assembly was used to identify the nonlinearity localized in the pylon when the thin beam contacts the surrounding support blocks. A penalty spring element was used to describe this nonlinear contact behavior and produced frequency backbone curves that agreed well with measured results. This model was validated through comparison of displacement response from stepped-sine simulations to those measured during the previous tests. A nonlinear reduced order model of the next-level assembly comprising of the pylon, wing, and fixture block was created using this calibrated nonlinear pylon model to generate pre-test predictions in the form of frequency-energy curves for the first two nonlinear normal modes. These were both shown to have internal resonances due to the dynamics of the next-level assembly, providing valuable insight into the design of future experiment and potential nonlinear phenomena to be observed in the data.

The results presented on the wing-pylon-fixture reveal the complex physics associated with the dynamics of the next-level assembly and fixturing. The NNM framework combined with nonlinear system identification can serve as a useful design tool to understand potential regimes in response when modes can interact. Depending on the objective of the structure, the tools utilized throughout this study can be used to tailor the dynamics of the system

for the intended needs, i.e. either exploit or eliminate the modal interactions. Future work will seek to validate these findings on test hardware with a variable length wing.

ACKNOWLEDGEMENTS

This research was conducted at the 2020 Nonlinear Mechanics and Dynamics (NOMAD) Research Institute supported by Sandia National Laboratories and hosted by the University of New Mexico. This paper describes objective technical results and analysis. Any subjective views or opinions that might be expressed in the paper do not necessarily represent the views of the U.S. Department of Energy or the United States Government. Supported by the Laboratory Directed Research and Development program at Sandia National Laboratories, a multimission laboratory managed and operated by National Technology and Engineering Solutions of Sandia LLC, a wholly owned subsidiary of Honeywell International Inc. for the U.S. Department of Energy's National Nuclear Security Administration under contract DE-NA0003525. The authors would like to thank Amy Chen of Sandia National Laboratories for her efforts in created the finite element meshes used throughout this study.

REFERENCES

[1] Butlin, T., Woodhouse, J., & Champneys A.R. (2015). The landscape of nonlinear structural dynamics: an introduction. Phil. Trans. R. Soc. A. 373: 20140400. http://doi.org/10.1098/rsta.2014.0400

[2] Noel, J.P. & Kerschen, G. (2017). Nonlinear system identification in structural dynamics: 10 more years of progress. *Mechanical Systems and Signal Processing*, Vol. 83.

[3] Cooper, S.B., et al. (2020). Investigating Nonlinearities in a Demo Aircraft Structure Under Sine Excitation. Cham: Springer International Publishing.

[4] Cooper, S.B., DiMaio, D., & Ewins, D. J. (2017). Integration of system identification and finite element modelling of nonlinear vibrating structures. *Mechanical Systems and Signal Processing*, Vol. 102.

[5] Ligeikis, C., et al. (2020). Modeling and Experimental Validation of a Pylon Subassembly Mockup with Multiple Nonlinearities. *38th International Modal Analysis Conference (IMAC XXXVIII)*, Houston, TX.

[6] Hurty, W.C. (1965). Dynamic Analysis of Structural Systems Using Component Modes. *AIAA Journal*, Vol. 3, No. 4, 678-685.

[7] Craig, R.R., Jr. & Bampton, M.C.C. (1968). Coupling of Substructures for Dynamic Analysis. *AIAA Journal*, Vol. 6, No. 7, 1313-1319.

[8] Kerschen, G., Peeters, M., Golinval, J.C. & Vakakis, A.F. (2009). Nonlinear normal modes, Part I: A useful framework for the structural dynamicist. *Mechanical Systems and Signal Processing,* vol. 23, no. 1, pp. 170-194, 10.1016/j.ymssp.2008.04.002.

[9] Krack, M. & Gross, J. (2019). Harmonic Balance for Nonlinear Vibration Problems. 10.1007/978-3-030-14023-6.

[10] Craig, R.R., Jr. & Kurdila, A.J. Fundamentals of Structural Dynamics. Second Edition. John Wiley & Sons. Inc., 2006.

[11] Sierra Structural Dynamics Development Team (April 2020). Sierra/SD – User's Manual – 4.56. SAND2020-3028.

[12] Peeters, M., Viguie, R., Serandour, G., Kerschen, G., & Golinval, J.C. (2009). Nonlinear normal modes, Part II: Toward a practical computation using numerical continuation techniques. *Mechanical Systems and Signal Processing,* vol. 23, no. 1, pp. 195-216, 10.1016/j.ymssp.2008.04.003.

[13] CUBIT Development Team. CUBIT 15.6 User Documentation. SAND2020-4156 W.

[14] Segalman, D.J. (2006). Modelling joint friction in structural dynamics. *Structural Control Health Monitoring*, Vol. 13, No. 1, pp. 430–453.

[15] Peeters, M,. Kerschen, G. & Golinval, J.C. (2011). Dynamic testing of nonlinear vibrating structures using nonlinear normal modes. Journal of Sound and Vibration. 330. Pp. 486-509. 10.1016/j.jsv.2010.08.028.